International Journal of Biological Macromolecules 286 (2025) 138003

Contents lists available at ScienceDirect

International Journal of Biological Macromolecules

journal homepage: www.elsevier.com/locate/ijbiomac

Structural dynamics of calcium and integrin-binding protein 2 (CIB2) reveal uncommon flexibility and heterogeneous calcium and magnesium loading

Gabriele Olivieri [a,1], Giuditta Dal Cortivo [b,1], Rebecca Dal Conte [a], Serena Zanzoni [c], Valerio Marino [b], Daniele Dell'Orco [b,*], Francesca Cantini [a,*]

[a] Magnetic Resonance Center, Department of Chemistry, University of Florence, Sesto Fiorentino, Italy
[b] Department of Neurosciences, Biomedicine and Movement Sciences, Biological Chemistry Section, University of Verona, Verona, Italy
[c] Centro Piattaforme Tecnologiche, University of Verona, Verona, Italy

ARTICLE INFO

Keywords:
Calcium sensor protein
Nuclear magnetic resonance
Molecular dynamics

ABSTRACT

Calcium- and Integrin-Binding protein 2 (CIB2) is a widely expressed protein with an uncertain biological role. Two of its four EF-hand motifs bind Mg(II) and/or Ca(II), thus triggering conformational changes. Although previous studies suggested that CIB2 preferentially binds Mg(II) over Ca(II) under physiological conditions, an atomic level characterization of CIB2 in the presence of both cations was lacking. Based on a combination of solution NMR, exhaustive molecular dynamics simulations and isothermal titration and differential scanning calorimetry, we characterized the interaction of CIB2 with both Ca(II) and Mg(II) ions and elucidated the protein regions involved in the interaction with the α7B integrin target. Analysis of experimental amide nitrogen relaxation rates shows that the EF4 motif exhibits high mobility regardless of the specific bound metal ion and demonstrates that the Mg(II)- and Ca(II)-bound state of CIB2 is relatively floppy, with pico-nanosecond motions induced in a region involved in target recognition. Overall, our data indicate a preferential, thermodynamically stable but structurally flexible state for CIB2, in which a Mg(II) ion is bound to EF3 and a Ca(II) ion to EF4. These results unveil the role of metal binding events in CIB2 and offer new insights into the dynamic regulation of target recognition.

1. Introduction

The Calcium and Integrin Binding (CIB) protein family consists of four genes encoding distinct proteins in the human genome, namely CIB1, CIB2, CIB3, and CIB4, which share structural characteristics [1–3] and are evolutionarily related to the Neuronal Calcium Sensor (NCS) family [4] (see Fig. 1 for a sequence alignment of the four CIBs). The human *CIB2* gene (NG_033006) encodes four different isoforms composed of 4-6 exons [5]. The canonical sequence (Uniprot code: O75838-1) encodes a 187-amino-acid protein (CIB2) with a molecular weight of 21.6 kDa, containing two functional EF-hands, a helix-loop-helix metal-binding motif that defines the largest family of calcium binding proteins in eukaryotic cells [6]. It is well-established that the C-terminal domain accommodates the functional EF-hands of CIB2 (EF3 and EF4), while the nonfunctional EF1 and EF2 motifs are located in the N-terminal domain (Fig. 1). Although the three-dimensional structure of CIB2 is currently unknown, homology models have been developed based on the experimental structures of CIB1 [7] and CIB3 [3] and have been used to interpret some biochemical and biophysical data.

CIB2's broad expression across various tissues in different organisms (see [8] for a recent review) indicates its involvement in a wide range of biochemical processes. Initially, the biological role of CIB2 was linked to its interaction with specific integrins involved in intracellular and extracellular signaling pathways [9,10]. Specifically, the αIIbβ3 integrin was found to be a shared target between CIB1 and CIB2 in platelets and megakaryocytes, where CIB2 can compensate for the absence of CIB1 [9]. In contrast, α7Bβ1D integrin seems to be specific for CIB2 in skeletal muscles, and both proteins were found to be downregulated in a congenital muscular dystrophy type 1A mouse model [10]. More recent evidence has connected CIB2 with hearing physiology and pathology [11]. Some lines of evidence support a pivotal role for CIB2 in stereocilia functioning and maintenance [12,13], while some other studies conclude that CIB2 is essential for the localization and function of the mechanotransduction channel [3], working as an intimal channel

* Corresponding authors.
E-mail addresses: daniele.dellorco@univr.it (D. Dell'Orco), francesca.cantini@unifi.it (F. Cantini).
[1] These authors contributed equally and should be considered co-first authors.

https://doi.org/10.1016/j.ijbiomac.2024.138003
Received 25 September 2024; Received in revised form 20 November 2024; Accepted 22 November 2024
Available online 23 November 2024

Fig. 1. Multiple amino acid sequence alignment of CIB family members performed by T-Coffee (https://tcoffee.crg.eu/apps/tcoffee/index.html). EF-hand motifs 1 to 4 are represented with graphical elements (BioRender) and colored in orange, green, cyan and purple, respectively. Amino acids involved in Ca(II) coordination are indicated in bold and labeled according to the canonical pentagonal bipyramidal geometry. Residues directly involved in the interaction with the α7B_M target peptide (aa. 138-148; see Section 3.7) are framed in red.

component by interacting with TMC1 [3] and BAIAP2L2 [14]. Cellular localization studies identified CIB2 on the tips of mature stereocilia of outer hair cells, inner hair cells and vestibular explants [15], indeed, so far, up to 13 point mutations in the gene encoding for CIB2 have been associated with sensorineural hearing loss [8]. Concurrently, biochemical and biophysical studies [2,7,16] highlighted both similarities and significant differences between CIB2 and other members of the CIB family. These distinctions should be taken into account when exploring CIB2's versatile yet largely unknown functions and its involvement in diverse processes such as autophagy [17], cancer [18], and muscular dystrophy [10].

Since its discovery and due to its similarity with CIB1, CIB2 was anticipated to function as a calcium sensor, capable of regulating specific molecular targets as a consequence of the conformational change induced by the binding of Ca(II) ions, and potentially other cations. Studies on heterologously expressed and purified human CIB2 indeed proved that the protein undergoes a pronounced conformational change upon Ca(II) binding, as expected by a typical EF-hand calcium sensor. The exposure of a hydrophobic region increases the α-helix content in CIB2's secondary structure, as demonstrated by far-UV Circular Dichroism (CD) spectroscopy [2]. Notably, Nuclear Magnetic Resonance (NMR) spectroscopy (^{1}H-^{15}N-HSQC NMR) revealed that in the absence of cations (apo-state), CIB2 adopts a disordered structure, while far-UV CD spectroscopy confirmed the presence of residual α-helix secondary structure, consistent with a molten globule state, as highlighted as well by near-UV CD spectroscopy [7]. Upon the addition of either Mg(II) or Ca(II), CIB2 was shown to adopt a well-ordered tertiary structure, although the apparent affinity for Ca(II) of CIB2 was significantly lower compared to that of CIB1, which raises doubt on its biological function as cytoplasmic calcium sensor [2,7]. Although informative on the peculiar characteristics of CIB2, it should be noted that previous NMR studies did not include specific chemical groups assignments, therefore a detailed atomic structure of CIB2 is not available, nor is a thermodynamic characterization of the binding process of Ca(II) and Mg(II) to the EF-hand motifs of the protein.

In this study, we aim to fill the existing gaps in structural knowledge regarding CIB2 and its interactions with Ca(II) and Mg(II) ions, with the ultimate goal of defining physiologically relevant signaling states and offering insights that clarify the protein's unique properties in calcium signaling and molecular target recognition.

2. Materials and methods

2.1. Protein expression and purification

The cDNA of CIB2 (Uniprot entry: O75838-1) was inserted into a PET24a(+) plasmid, resulting in a construct encoding for a 189 residue protein. The plasmid was used to transform *E. coli* BL21 (DE3) arctic competent cells. Cell growth was performed in M9 (3.0 g/l ^{13}C-D-glucose and 1.2 g/l $^{15}NH_4Cl$) medium added with Q solution and Mohr's Salt at 37 °C. When the culture reached an OD_{600} of 0.4, the temperature was lowered to 15 °C in an ice bath. When culture reached an OD_{600} of 0.6, 0.5 mM IPTG was added to induce protein overexpression, and the cells were incubated at 15 °C for 20 h. Harvested cells were re-suspended in 20 mM Tris (pH 7.5), 0.5 M NaCl, 20 mM imidazole, 1 mM DTT, 2.5 mM Mg(II), 0.1 mg/ml lysozyme, 5 U/ml DNAse and 1 X protease inhibitor cocktail, incubated at room temperature for 20 min and mechanically lysed via sonication on ice (15 min, 2 s pulses at 3 s intervals). After lysis, the inclusion bodies were separated by centrifugation for 30 min at 4 °C 18,000 × g, resuspended in 6 M guanidine-HCl and incubated overnight at 4 °C. The soluble fraction was separated by centrifugation for 30 min at 4 °C 18,000 × g and loaded onto a HisTrap FF crude column (GE Healthcare) previously loaded with Ni(II). Unfolded His-CIB2 was refolded via a descending guanidine-HCl gradient (6 M to 0 M in 100 ml at 1 ml/min) and purified via a one-step elution with 20 mM Tris pH 7.5, 150 mM NaCl, 500 mM imidazole. His-CIB2 was subsequently dialyzed against 20 mM Tris pH 7.5, 150 mM NaCl, 1 mM DTT to remove imidazole and incubated at room temperature overnight with ProTEV protease (Promega, 1 U for 200 μg protein). Finally, the sample was reloaded onto the HisTrap FF crude column to remove the 6xHis-tag and collect purified CIB2 from the flowthrough. Samples for ITC and DSC measurements were exchanged against 20 mM Tris-HCl pH 7.5, 150 mM

KCl, 1 mM DTT, flash-frozen and stored at -80 °C, while those for NMR triple resonance experiments and heteronuclear relaxation NMR experiments were exchanged against 20 mM Hepes, 150 mM NaCl, 1 mM DTT, pH 7.5.

2.2. NMR spectroscopy for backbone assignment

NMR experiments used for resonance backbone assignment of CIB2 in the presence of 4 mM Mg(II) were recorded on Bruker NMR spectrometers on 0.3 mM ^{13}C-^{15}N-labeled samples. All NMR spectra were collected at 298 K, processed using Topspin 4.0.6 (Bruker) and analyzed through CARA [19]. Protein samples were added with 10 % D_2O and $MgCl_2$ or $CaCl_2$ up to a protein:metal ion molar ratio of 1:20. For the backbone resonance assignments of diamagnetic signals, we recorded ^{1}H detected ^{15}N- and ^{13}C-HSQC, HNCA, HNCO, HNCOCA, and CBCACONH. The parameters used are reported in Supplementary Table ST1.

Proton resonances were calibrated with respect to the signal of 2,2-dimethylsilapentane-5-sulfonic acid (DSS). Nitrogen chemical shifts were referenced indirectly to the ^{1}H standard using a conversion factor derived from the ratio of NMR frequencies. Carbon resonances were calibrated using the signal of dioxane at 69.4 ppm (298 K) as secondary reference. The resonances assignment of MgMg-CIB2 was deposited in BMRB (https://bmrb.io/; entry 52609). It should be noted that in our protein construct the numbering is such that Met 1 of UNIPROT (O75838 * CIB2_HUMAN) is Met 3 in our construct numbering.

The backbone chemical shifts of MgMg-CIB2 were used as input to run the program Talos-N [20], which provided the prediction of the secondary structure content.

2.3. NMR titration of CIB2 with Mg(II) and Ca(II)

We titrated the ^{15}N labeled CaCa-CIB2 (protein concentration = 60 μM, in the presence of 1.2 mM Ca(II); pH 7.5) by adding six aliquots of a Mg(II) solution, starting from a [Mg(II)] concentration of 15 μM to a final concentration of 0.84 mM. For each titration point we acquired an ^{1}H-^{15}N-HSQC experiment at 298 K on Avance 900 Bruker spectrometer operating at proton nominal frequency of 899.1 MHz. We repeated the NMR titration on ^{15}N labeled MgMg-CIB2 (protein concentration = 60 μM, in the presence of 1 mM Mg(II); pH 7.5) by adding ten aliquots of a Ca(II) solution starting from a concentration of 15 μM to 2.4 mM, with the same buffer condition. For both NMR titrations, the NMR spectra were processed and integrated with Bruker Topspin 4.0.6 software (Bruker) by applying a square cosine bell apodization on both dimensions, and analyzed by CARA program [19]. The combined chemical shift variations were calculated for each assigned residue through the following equation:

$$\Delta\delta^{combined} = \sqrt{\frac{(\Delta\delta(^{1}H))^2 + \frac{1}{25}(\Delta\delta(^{15}N))^2}{2}} \quad (1)$$

The resonances assignment of CaCa-CIB2 was deposited in BMRB (52608 code).

2.4. $^{1}H_N$-relaxation experiments

Measurements of heteronuclear ^{15}N longitudinal (R_1) and transversal ($R_{2)}$ relaxation rates and {^{1}H}-^{15}N NOEs on MgMg-CIB2 and MgCa-CIB2 were carried out using 11.7 T Bruker AVANCE 500 equipped with a triple resonance, inverse detection, cryoprobe (TXI) using a sample of 240 μM and 200 μM for MgMg-CIB2 and MgCa-CIB2, respectively. The experiments were acquired with recycle delays (d_1) of 3 s for R_1 and R_2 and 5 s for {^{1}H}-^{15}N NOE. A series of twelve ^{15}N-R_1-HSQC experiments were recorded using a period of 0.010 s, 0.04 s, 0.08 s, 0.125 s, 0.200 s, 0.370 s, 0.500 s, 0.675 s, 0.800 s, 1 s, 1.55 s and 2.5 s. For each experiment, 16 scans were collected over 128 increments.

A series of eleven ^{15}N-R_2-HSQC experiments were recorded using period of 8.48 ms, 16.96 ms, 33.92 ms, 50.88 ms, 67.84 ms, 101.76 ms, 135.64 ms, 152.64 ms, 186.56 ms, 203.52 ms and 220.48 ms. For each experiment, 64 scans were collected over 128 increments.

Amide resonances were integrated using CARA [19] and the T_1 ($1/R_1$) and T_2 ($1/R_2$) values were obtained by fitting peak intensities using single exponential decay:

$$I(t) = I_0 exp\left(-\frac{t}{T_{1,2}}\right) \quad (2)$$

where $I(t)$ is the peak intensity, t is the time, and I_0 is the intensity at time 0 using ORIGIN software. The analysis of the uncertainties of the R_1 and R_2 values was carried out by comparing the peak heights on duplicate spectra at 10 ms (shortest value of relaxation delay). The heteronuclear steady-state {^{1}H}-^{15}N NOE values were obtained from the ratios of peak intensities in the saturated spectrum to those in the unsaturated spectrum.

The average backbone ^{15}N R_1 and R_2 relaxation rates and {^{1}H}-^{15}N NOEs values for MgMg-CIB2 were 1.3 ± 0.1 s^{-1}, 19.1 ± 2.9 s^{-1} and 0.7 ± 0.1, respectively, while the average backbone ^{15}N R_1 and R_2 relaxation rates for MgCa-CIB2 were 1.3 ± 0.2 s^{-1}, 17.8 ± 4.0 s^{-1}, respectively.

For the model-free analysis we used Dynamics Center (https://www.bruker.com/it/products-and-solutions/mr/nmr-software/dynamics-center.html), a comprehensive software solution for relaxation, diffusion, and kinetics analyses, which uses NMR data and one or two non-frequency dimensions to perform automated and semi-automated analysis. In the model-free approach R_1, R_2 and {^{1}H}-^{15}N NOE are taken together to provide a description of the dynamic properties of each residue, considering the anisotropy and the overall correlation time (τ_c) of the molecule, which are automatically calculated by the program. The ratio of the parallel and perpendicular diffusion coefficients $D_{//}/D_{\perp}$ resulted from the model-free analysis was 1.48, therefore we assumed an anisotropic tumbling for our analysis. Based on this key parameter value, five parameter sets were fitted to the anisotropic diffusion model in order to interpret the NMR relaxation data. The order parameters characterizing the internal mobility have been determined within the Lipari-Szapo model. The order parameter (S^2) describes the magnitude of the angular oscillation of a chemical bond vector such as the amide bond in proteins, reflecting the flexibility of the polypeptide at those sites with respect to the overall protein frame [21,22]. For $S^2 = 0$, the internal motion spans all possible orientations, whereas $S^2 = 1$ corresponds to complete rigidity [23].

The overall correlation time (τ_c), as estimated from the R_2/R_1 ratios, was 14.4 ± 1.1 ns for MgMg-CIB2, and 14.6 ± 1.2 ns for MgCa-CIB2, in line with the value calculated by HYDRONMR [24] on the monomeric protein (14.1 ns).

2.5. Alphafold2

Alphafold2 is a neural network-based approach to predict protein structures with atomic accuracy [25,26]. The AlphaFold2 network directly predicts the 3D coordinates of all heavy atoms for a given protein using the primary amino acid sequence and aligned sequences of homologues as inputs. Using the Alphafold2 interface provided by Neurosnap opensource platform, we obtained 5 models with a 0.47 Root-Mean Square Deviation (RMSD) value. The mean predicted Local Distance Difference Test value (pLDDT), which is an accurate descriptor of tertiary model quality, falls, for each model, in a range between 90.15 and 85.67. Lower pLDDT values were obtained for residues located at the C-terminal region (residues 172-189). The Predicted Aligned Error value (PAE), which indicates the reliability of the predicted relative position and orientation of one residue with respect to the others [26,27], was around 30 Å only for a few residues at the N- and C-termini, while for those belonging to secondary structure elements, the average PAE value remained below 10 Å, demonstrating good overall prediction of the tertiary structure [26].

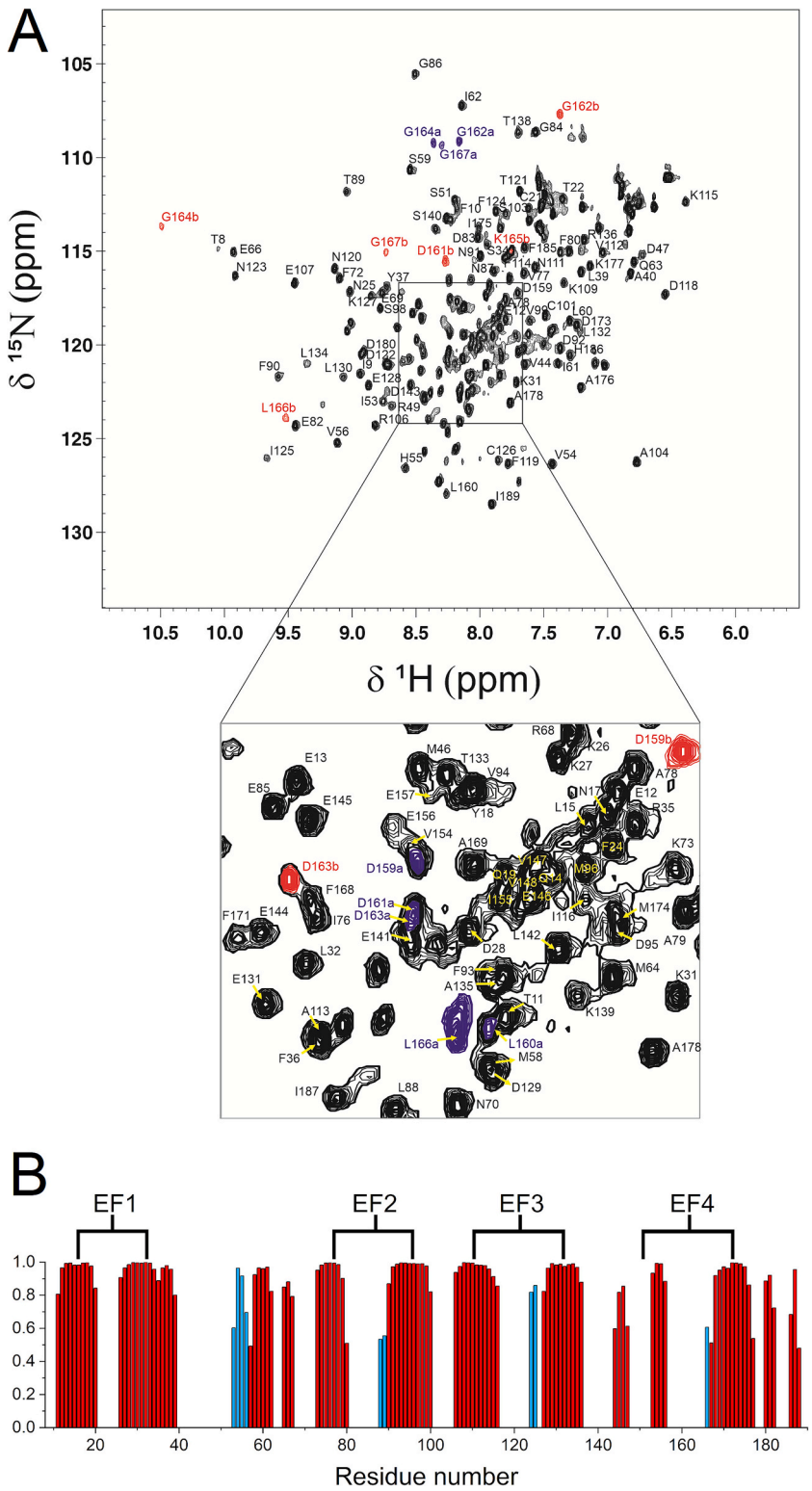

Fig. 2. A) $^{1}H^{15}N$ HSQC spectrum of CIB2 in the presence of 4 mM Mg(II). Resonances for the EF4 region assigned to the MgMg-CIB2 form are colored in red and labeled with letter "b", those assigned to the MgE-CIB2 form in blue and labeled with letter "a", where MgE indicates that EF4 does not bind any cation. A spectral region has been amplified to facilitate the analysis. B) Secondary structure prediction from the assigned chemical shifts using TALOS-N. β-Sheet and α-helical probability is plotted with blue and red bars, respectively. The EF domains are labeled.

2.6. CYANA

During the CYANA calculation we included the metal ions by appending a chain of linker residues to the amino acid sequence [28,29]. At the end of the linker, two atoms with a radius mimicking the target Mg(II) ions were added. The linker residues had pseudo-atoms with van der Waals radii set to zero. The atoms of the ligands, predicted from [8], can be linked to the Mg(II) ions through upper and lower distance limits. With this approach, which has been used for MgMg-CIB2 structure calculation, the two Mg(II) ions were located within the EF3 and EF4

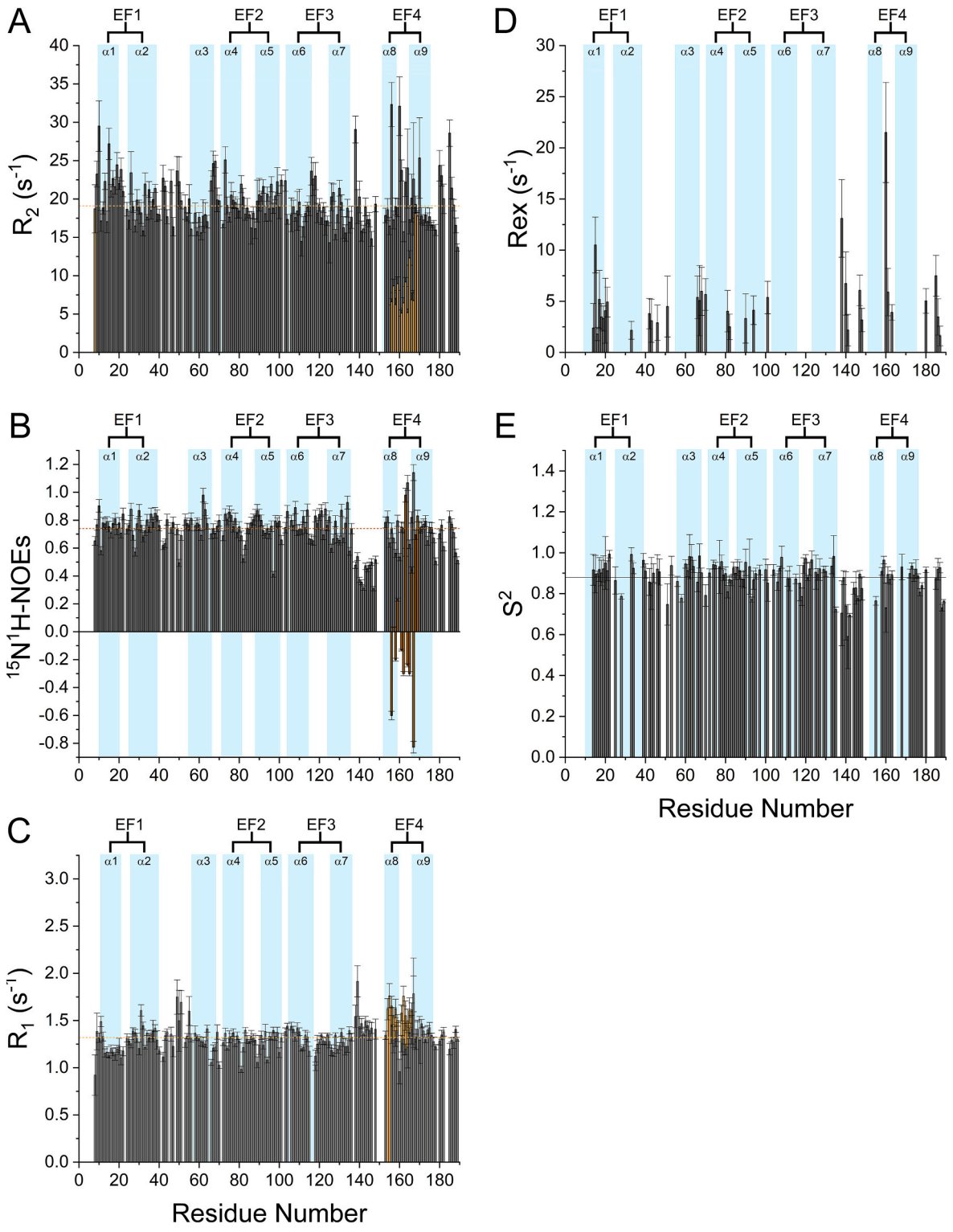

Fig. 3. NMR relaxation measurements. A) ^{15}N R_2 relaxation parameters; B) {^{1}H}-^{15}N NOE heteronuclear; and C) ^{15}N R_1 recorded at 500 MHz versus the residue numbers for CIB2 in the presence of 4 mM Mg(II) in 20 mM Hepes, 150 mM NaCl, 1 mM DTT, pH 7.5 and 10 % D_2O. The residues experiencing mobility on a wide range of timescale are labeled in red. D) Rex contribution to ^{15}N R_2 values. E) Order parameters versus residue numbers. Tdomains are also labeled.

binding sites.

2.7. NMR titration with alpha 7b peptide

The peptide (α7B_M) encompassing the 1101–1116 membrane proximal region of the cytoplasmic domain of α7B integrin (Uniprot entry: Q13683; Ac-LLLWKMGFFKRAKHPE-NH_2) was synthesized by GenScript, with a final purity ≥95 % as tested by HPLC. The peptide was dissolved in DMSO to improve solubility, taking care of adding small volumes to ensure a maximum amount of 2 % DMSO (v/v) in the NMR sample solution. One hundred micromolar CIB2 was titrated with 1:0.5, 1:1, 1:2 equivalents of DMSO-dissolved peptide. In parallel, a titration

including sole DMSO was performed to estimate the influence of the solvent on the chemical shifts. No significant change in the backbone amide was found with concentration of DMSO ≤2 %.

2.8. Differential scanning calorimetry

Thermal denaturation of CIB2 in the absence and presence of metal ions was carried out using a nano-DSC (TA instrument) with a cell volume of 300 μl. The protein was dissolved in 20 mM Tris pH 7.5, 150 mM NaCl at pH 7.5 in the presence of either: i) 1 mM EDTA; ii) 1 mM Mg(II) or Ca(II); iii) both. Scans were performed in a 5–65 °C range at a scan rate of 60 °C h^{-1} and the data were fitted according to a two-state model using NanoAnalyze software (TA instrument).

2.9. Isothermal titration calorimetry

Isothermal Titration Calorimetry (ITC) experiments were performed at 25 °C using a MicroCal PEAQ-ITC instrument (Malvern, UK). A thorough and effective protein/buffer decalcification protocol was performed as explained in refs. [30,31] to obtain apo-CIB2 (residual calcium below 1 μM). Apo CIB2 was placed in the sample cell at a protein concentration of 38 or 76 μM, while the titrant cations, Mg(II) or Ca(II), were placed in the titration syringe at 10 mM. For competition experiments, the protein in the sample cell was pre-incubated with the metal ion at a molar ratio of 8:1 (ligand:CIB2). Titrations were performed by an initial injection of 0.2 μl, followed by 39 injections of 1 μl. The time interval between injections was 120 s and stirring speed was set at 500 rpm with a low feedback mode. The data were analyzed using the MicroCal PEAQ-ITC Analysis software using "one set of sites" binding model.

2.10. Molecular modeling of CIB2 under different ion-loading conditions

The refined structural model of MgMg-CIB2 obtained in this study was used as template to generate three ion-loading states of CIB2: i) 2 Mg (II) ions bound to EF3 and EF4, respectively (MgMg); ii) 2 Ca(II) ions bound to EF3 and EF4 (CaCa), and iii) a Mg(II) ion bound to EF3 and a Ca(II) ion bound to EF4 (MgCa). The three CIB2 models were built by replacing the ions bound to the two functional EF-hands EF3 and EF4, then prepared using the *Protein Preparation Wizard* protocol provided by Bioluminate (Schroedinger), which consisted in: i) assigning bond orders based on the Chemical Components Dictionary database (www.pdb.org, wwPDB Foundation, Piscataway, NJ, USA); ii) addition of H atoms; iii) prediction of the protonation states of ionizable residues at pH 7.4 using PROPKA [32]; iv) assignment and optimization of H-bonds; v) minimization of the modelled structures using OPLS4 as force field (Schroedinger, New York, NY, USA) and 0.3 Å as threshold for the RMSD of heavy atoms.

2.11. Molecular dynamics simulations of CIB2

The three ion-loading states of CIB2 described in the previous section were subjected to Molecular Dynamics simulations on GROMACS 2016.5 [33], using the all-atom forcefield CHARMM36m [34]. CIB2 structures were centered in a dodecahedral simulation box where the edges were located 1.2 nm far from any protein atom to avoid artifacts due to the interaction with neighboring periodic images. After filling simulation boxes with water molecules, the systems, consisting of approximately 54,000 atoms, were neutralized with 150 mM KCl, minimized according to a two-step protocol based on steepest descent and conjugate gradients [35], and equilibrated in NVT ensemble at 310 K for 2 ns with position restraints and for other 2 ns with no position restraints, as described in [36]. Finally, the three systems were simulated at constant temperature (310 K) and pressure (1 atm) for 1 μs using the setup elucidated in [37]. The overall consistency of the trajectories was assessed by monitoring the evolution of the Cα-RMSD over the simulated timeframe, while the flexibility of the three CIB2 systems was assessed by monitoring the Root-Mean Square Fluctuation (RMSF) of the Cα atoms, representing the time-averaged RMSD with respect to their average position. Similarly, the RMSF was also calculated on the two ions bound to EF3 and EF4 in the three ion-loading states to evaluate each ion's propensity to fluctuate within the binding loop, indicative of differences in the optimal geometry necessary for ion coordination. RMSD, RMSF and distances were calculated using the *gmx rms*, *gmx rmsf*, and *gmx distance* functions provided by GROMACS 2016.5, respectively.

The representative structure of the trajectory of the three CIB2 forms was obtained first by clustering the conformations of each ns of the trajectory. Then, the structure with the lowest RMSD with respect to all other structures within the same ns was selected as representative for the specific ns of the trajectory, yielding a representative trajectory constituted by 1000 frames. Finally, a second round of clustering of the 1000 representative conformations allowed the identification of the representative structure of the entire trajectory.

Interhelical angles between helices α6 and α7 of the EF3 motif in the structural models of CIB2 and Mg(II)-bound CIB1 and Ca(II)-bound CIB1 [38] were calculated using Chimera [39].

3. Results and discussion

3.1. NMR characterization of Mg(II)-CIB2 reveals high structural flexibility in the EF4 region

The ^{1}H-^{15}N HSQC spectrum of CIB2 in the presence of 4 mM Mg(II) showed overall dispersed resonances indicative of a well folded protein (Fig. 2A). The analysis of the NMR experiments allowed us the assignment of about 92 % of backbone resonances of CIB2 protein. Residues which remained unassigned were G1-Q7, F23, Y48, E102, L149-C151, D170. Prediction of the secondary structure content as derived from the backbone chemical shifts (HN, Cα, Cβ, CO, N), using Talos-N program [20] revealed that the secondary structure of CIB2 in the presence of Mg(II) comprises nine α-helices and four short β-strands (Fig. 2B), which is consistent with the topologies of the homologous proteins CIB1 [38] and CIB3 [3]. In particular, in calcium- and integrin-binding proteins, eight of the nine helices participate in four EF-hand motifs (helix-loop-helix motif), typical of Ca(II) and Mg(II) binding proteins [40] and the two potential metal binding sites are located at the C-terminus and comprise helices α6 and α7 (EF3) and helices α8 and α9 (EF4) [8].

The analysis of the heteronuclear NMR relaxation experiments acquired on CIB2 in the presence of 4 mM Mg(II) shows that EF4 is dynamically active, while EF3 does not display significant dynamic motions (Fig. 3). Indeed, several residues of EF4 (residues V147, V148, L160, D161, D163) and at the C-terminal end (D180, F185, H186 and I187) experience Rex contribution to ^{15}N R_2 values, indicating the presence of conformational exchange processes in the μs-ms timescale (Fig. 3). Moreover, stretch 138-148, located in the loop proceeding helix α8, shows steady state {^{1}H}-^{15}N NOE values lower than average, typical of the presence of local motions in the ns-ps timescale. Accordingly, the order parameters (S^2) of these residues are lower than the average. Overall, these data demonstrate that the EF4 region and the loop between helices α7 and α8 are more flexible than EF3 region [7], and are affected by mobility on a wide range of timescales (Fig. 3). In agreement, the resonances of the Cα and Cβ atoms for many residues in the EF4 are missing in the triple resonance experiments, making the assignment very challenging. Some of these residues have been assigned indeed through backbone NOEs connectivity. This is also the reason why TALOS-N [20] was able to identify only the N- and C-terminal regions of the helix 8 (Fig. 2B). Previous limited proteolysis experiments assessed the sensitivity of metal cation-bound CIB2 to protease digestion [16], indirectly suggesting that some flexibility was present also in the cation-complexed state. The heteronuclear relaxation experiments here reported provide experimental evidence of such flexibility.

The atomic level characterization allows us to provide information

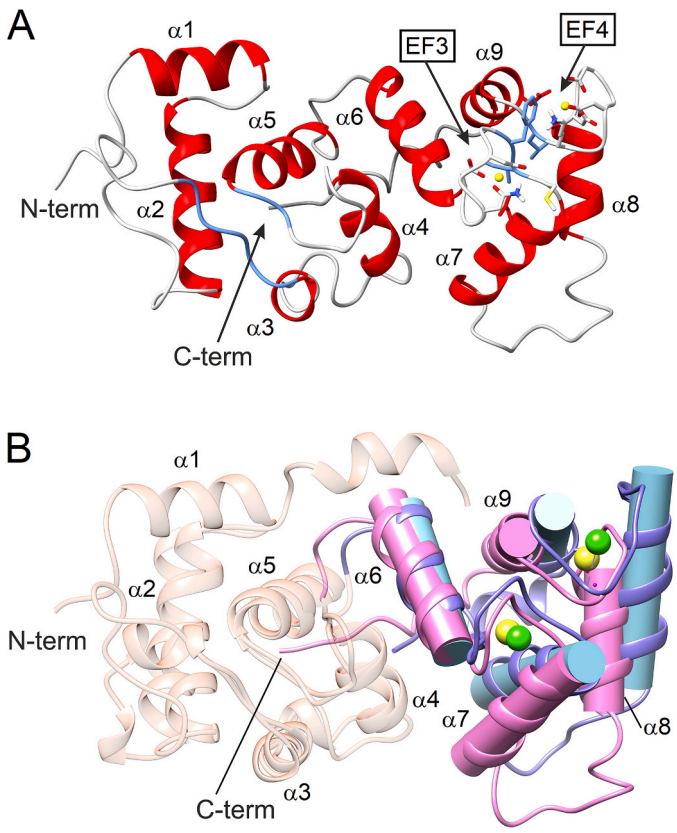

Fig. 4. A) CYANA-refined CIB2 three-dimensional backbone representation. α-helices are dyed in red and β-strands dyed in light blue. Two Mg(II) ions are bound to EF3 and EF4 binding sites in CIB2's C-terminal region and shown as yellow spheres. Ligand-binding residues' sidechains are shown. B) Overlay of the CYANA refined CIB2 three-dimensional structural model (pink ribbon) with the first conformer of the NMR family of the CaCa-CIB1 solution structure (PDB ID: 2L4H [38]) (light blue). Only the C-terminal domain is highlighted for sake of simplicity. The Ca(II) and the Mg(II) ions are shown as green and yellow spheres, respectively.

on another important region of CIB2, the E156-A169 stretch, which comprises the potential EF4 metal binding ligands, and displays two conformations in the ^{1}H-^{15}N HSQC spectrum in the presence of a large excess of Mg(II) (4 mM). We assigned one conformation to CIB2 with empty EF4 metal binding site and one Mg(II) atom bound to the EF3 site (hereafter named MgE-CIB2, where E stands for Empty site), while the second conformation was assigned to a state of CIB2, in which one Mg (II) ion is bound to EF3 and another one to EF4, hereafter named MgMg-CIB2. This assignment resulted from the analysis of both chemical shifts and heteronuclear relaxation data. Indeed, in the conformation assigned to MgE-CIB2, residues E156-A169 showed negative steady state {^{1}H}-^{15}N NOE values and transversal and longitudinal relaxation values R_2 and R_1 lower and higher respectively than the average (red bars in Fig. 3), indicating that this region displays motions typical of a random-coil conformation. The corresponding resonances of amide moieties suffer indeed from very poor dispersion of chemical shifts, supporting that these resonances belong to a not structured conformational state (Fig. 2A). These results are consistent with the fact that the E156-A169 stretch is not involved in metal binding and that the binding of Mg(II) in the EF3 site, although essential for the 3D folding of the protein [7], only partially stabilizes the EF4 site, which folds completely only upon binding of the metal ion. The amide resonances of E156-A169 residues in the conformation assigned to MgMg-CIB2 showed indeed larger chemical shift dispersion with respect to the MgE-CIB2 (Fig. 2A) and an increase of the steady state {^{1}H}-^{15}N NOE values (Fig. 3). The latter behavior shows that Mg(II) binding indeed triggers the folding of the EF4 metal binding site from a random coil conformation, although this region maintains high mobility even in the presence of the metal ion, as shown by the mobility data. It is worth noting that, at a CIB2:Mg(II) ratio of about 1:20 (4 mM Mg(II) in solution), the MgE-CIB2 state is still observed, and the molar fraction of MgMg-CIB2 is indeed 0.47 ± 0.1. Overall, this suggests that the EF4 binding site has a lower affinity for Mg(II) than EF3, which is instead fully occupied under these conditions, similarly to the behavior exhibited by CIB1, where Mg(II) can only occupy EF3, while leaving EF4 in intermediate conformational exchange between a Mg(II) bound and unbound state [41].

3.2. A three dimensional structural model for Mg(II)-bound CIB2

We generated five 3D structural models of CIB2 by Alphafold2 program [26], which displayed an overall Cα-RMSD of 0.34 Å (Fig. S1) with respect to one of the five models. The pLDDT values indicate that these 3D models have been predicted with high-confidence, except for the C-terminal region (stretch 172-189) for which the pLDDT values were lower than 80 [42]. In order to structurally refine the AlphaFold2 model, CYANA structure calculations were run following the protocol described in [43] including metal ions in the two EF3 and EF4 binding sites. Chemical shifts-derived dihedral angle restraints (φ and ψ angles) and NOEs restraints assigned in the C-terminal region were used to locate the two metal binding sites. The refined structural model of CIB2 (Fig. 4) shows that helix 8 is significantly shorter than the same helix in CIB1 structure [38,44], in agreement with the lack of experimental NMR restraints (Fig. S2). Interestingly, this is also the region for which the assignment of three backbone amide resonances is missing and also experience mobility in the ns-ps timescale.

3.3. NMR characterization of Ca(II)-CIB2: structural similarity but different occupation of the binding sites

The ^{1}H-^{15}N HSQC spectrum of CIB2 in the presence of 4 mM Ca(II) showed overall dispersed resonances, as observed for CIB2 in the presence of 4 mM Mg(II). The backbone assignment of the fully Ca(II)-loaded protein (CaCa-CIB2) was performed by comparing the ^{1}H-^{15}N HSQC resonances with those of MgMg-CIB2 and taking advantage of the analysis of 3D ^{1}H-^{15}N HSQC NOESY spectrum acquired on CIB2 in the presence of 4 mM Ca(II). At a CIB2:Ca(II) ratio of 1:20, the intensity of amide resonances of residues E156-A169 (corresponding to the empty EF4) were weaker than those observed in the presence of Mg(II) (Fig. S3). The molar fraction of CaCa-CIB2 specie was 0.90 ± 0.02 with respect to the CaE-CIB2, indicating that the EF4 binding site is almost completely occupied under these conditions, at odds with the analogous case in the sole presence of Mg(II). On the other hand, in repeated experiments we observed that CaCa-CIB2 gradually lost the metal ion bound to EF3 site, indicative of a lower affinity for Ca(II), which led to protein instability. Unfortunately, the inherent instability of the CaCa-CIB2 protein prevented us from conducting heteronuclear relaxation experiments necessary for the dynamic characterization of CaCa-CIB2.

The combined chemical shift differences between CaCa-CIB2 and MgMg-CIB2 showed that the protein regions affected by the presence of different metal ions are localized around the two metal binding sites EF3 and EF4, indicating that the overall global 3D structure is maintained regardless of the metals bound in the two sites (Fig. 5A). Altogether, the ^{1}H-^{15}N HSQC spectra showed that the overall structure of the fully metal-bound CIB2 is similar regardless of the cation bound in EF3, although EF4 is significantly more occupied in the presence of Ca(II).

These measurements show that the stoichiometric protein:cation ratio required to reach saturation in the first binding site is at least 1:20, while no complete saturation was observed for the second binding site. This is indicative of lower Ca(II) affinity for CIB2 compared to CIB1, as highlighted in previous studies [8], but it is not unexpected when considering its primary structure (see Fig. 1 for a comparison of the sequences). The structure of CIB1 [1] shows that an optimal pentagonal

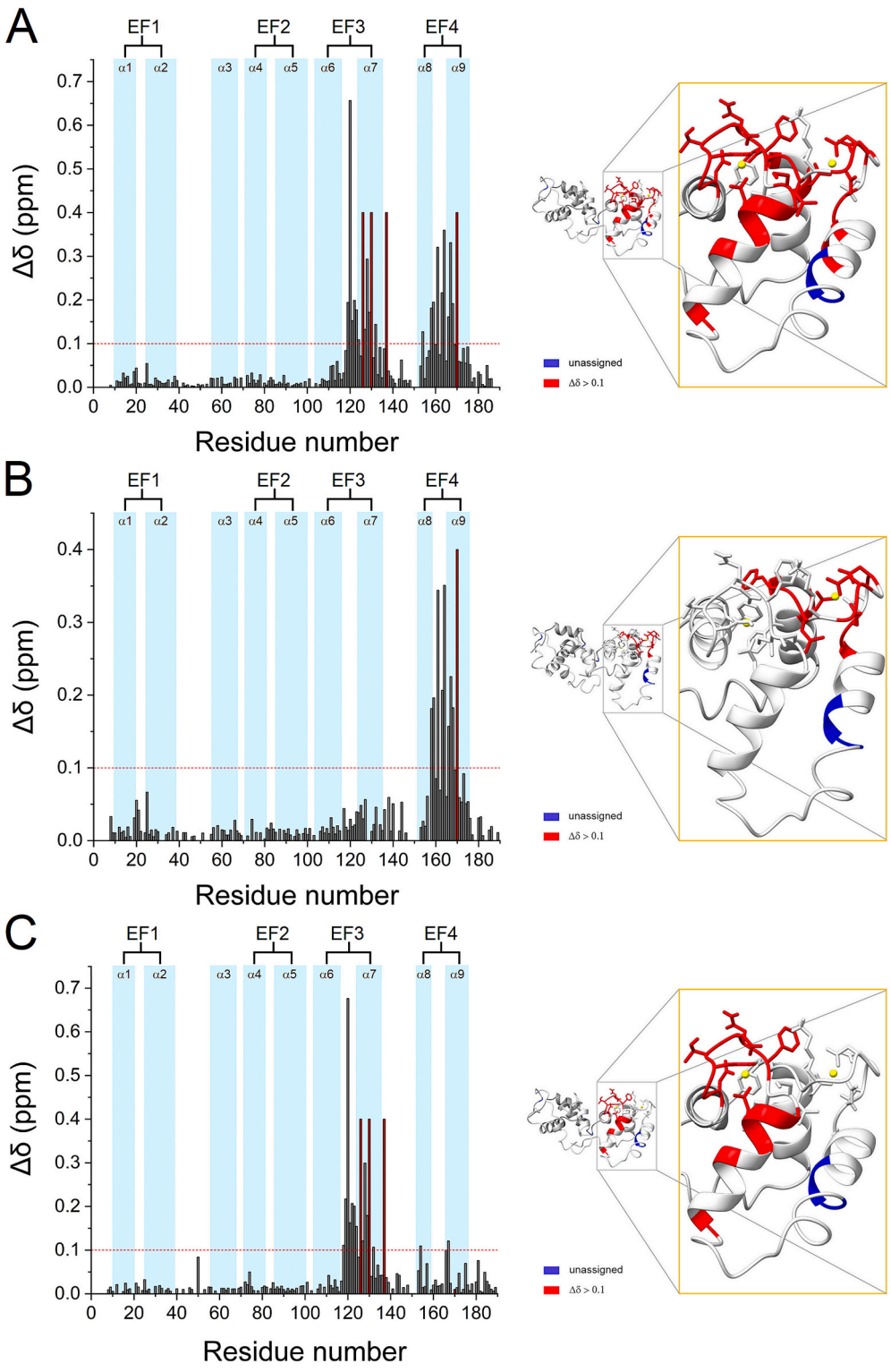

Fig. 5. Left: combined chemical shift differences between two different protein states recorded by ^{1}H-^{15}N HSQC experiments, against residue numbers. Red bars represent residues for which the chemical shift assignment is missing in one of the two species. The red dash lines indicate the chemical shift threshold value calculated as reported in [57]. Right: three-dimensional model representation zooming on the two metal ion binding sites. Red residues are affected by combined chemical shift >0.1 ppm. Blue residues are not assigned. A) Differences between MgMg-CIB2 and CaCa-CIB2 species; B) MgMg-CIB2 titrated with Ca(II); C) CaCa-CIB2 titrated with Mg(II).

bipyramid geometry is formed by oxygen-coordinating Ca(II) in EF4, which is facilitated by the presence of an Asn residue (N169) in the -X position of the coordinating loop and a Glu residue (E172) in the -Z position (Fig. 1). This Glu residue serves as a bidentate ligand for Ca(II), a feature that is widely conserved among EF-hand motifs [45,46]. In contrast, in CIB2, the -X and -Z positions are occupied by the side-chain-lacking G165 and D168, respectively, which cannot form a bidentate ligand due to the shorter side chain. This likely distorts the geometry of the loop and results in a lower affinity for Ca(II). Significant differences are also observed in EF3, which accounts for the reduced Ca(II) affinity

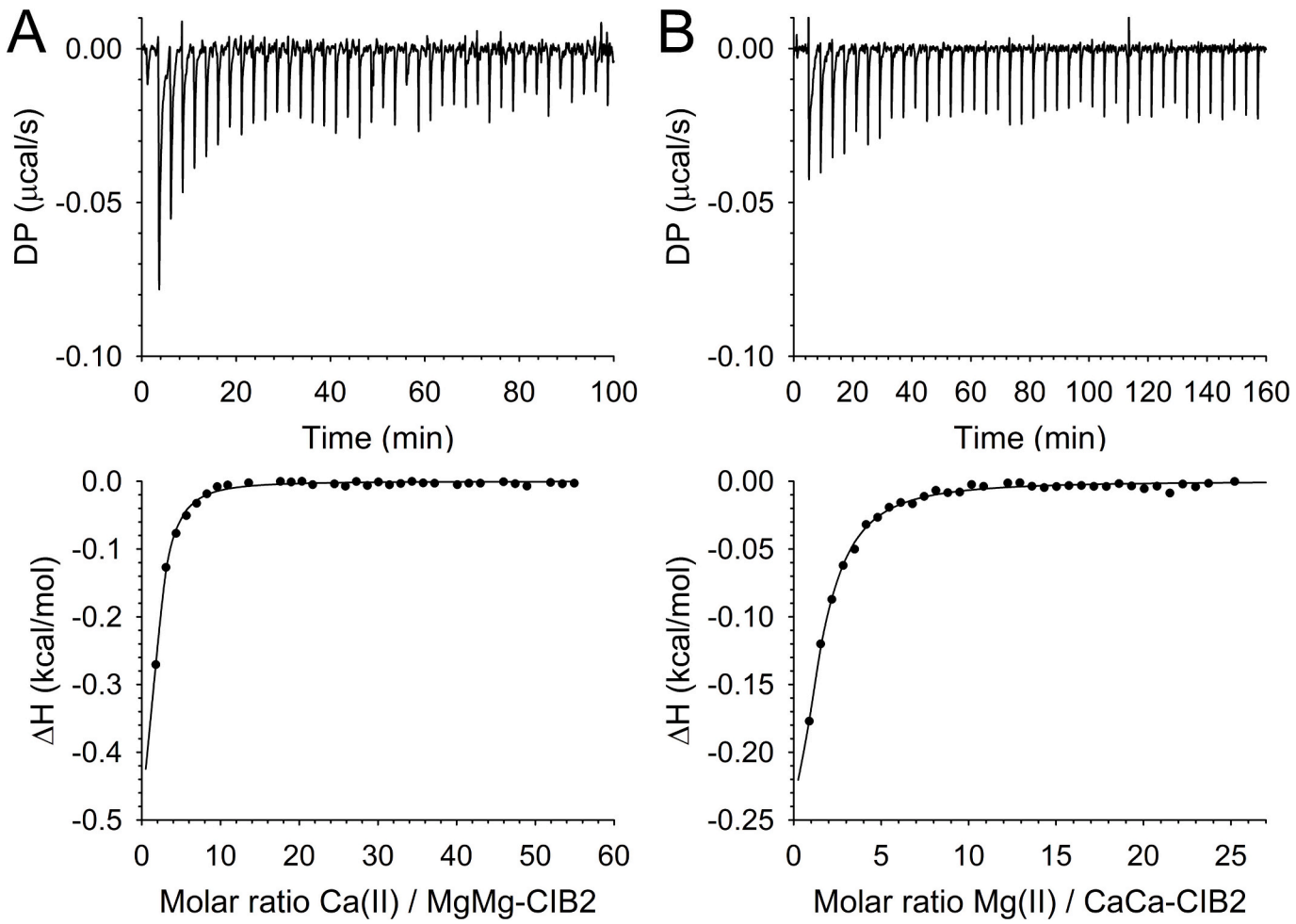

Fig. 6. Representative calorimetric titrations of Mg(II) and Ca(II) binding to CIB2. Raw heats (top panels) and binding isotherms (bottom panels) are shown for the titration of 38 or 76 μM CIB2 with A) 10 mM Ca(II) or B) 10 mM Mg(II) binding to the protein pre-incubated with 8-fold excess Mg(II) or Ca(II), respectively. The thermograms were fitted using the "one set of sites" model for competitive titration.

of this loop in CIB2 compared to CIB1. Moreover, in CIB1 the Y coordinating position is occupied by a negatively charged residue (D118), while in CIB2, a neutral residue (N118) is substituted, preventing favorable coulombic interactions. Additionally, the ninth position (-X) in the EF-hand loop is occupied by Asn (N124) in CIB1, but by the less commonly observed Cys residue (C124) in CIB2, a substitution known to destabilize some EF-hand structures [47]. To gain further insights into the structural differences between CIB2 and CIB1, and relate this to the lower affinity for Ca(II), we compared CIB2 structural models with the solution structure of CIB1 in its Ca(II)-bound (PDB: 2L4H [38], Fig. 4B) and Mg(II)-bound forms (PDB: 2L4I [38]). We noticed minor differences between the overall structure between CaCa-CIB1 and MgMg-CIB2, CaCa-CIB2, MgCa-CIB2, whose RMSD computed on Cα atoms resulted 1.28 Å, 1.35 Å and 1.20 Å respectively, while the same calculation could not be performed with respect to MgMg-CIB1 due to the missing C-terminal (residues 157-191). The main structural difference is the length of helix α8, which is significantly shorter than the corresponding helix in CaCa-CIB1 and MgMg-CIB1 structures. However, differences in the first coordination sphere may contribute to the lower affinity of CIB2 for cations and may also change interhelical angle between α6 and α7 in the EF3 motif. Indeed, we found that, in CaCa-CIB2 structural model such angle was 101.5° whereas in CaCa-CIB1 structure (PDB: 2L4H [38]) it was 122.8°, thereby indicating a different orientation of the two helices. Upon replacement of Ca(II) with Mg(II) in EF3 the interhelical angle increases up to 115.3°. Consequently, both the sequence and the structure of CIB2 are not evolutionarily optimized for pure Ca(II) binding.

3.4. Isothermal titration calorimetry and nuclear magnetic resonance show similar binding profiles for Ca(II) and Mg(II)

To further characterize the metal binding to CIB2, we performed Isothermal Titration Calorimetry (ITC) measurements, with the goal of estimating the thermodynamic parameters of the binding process, starting from the cation-free form (apo). While we could obtain reproducible exothermic thermograms upon titration of apo-CIB2 with both Ca(II) (Fig. S4A) and Mg(II) (Fig. S4B), the biphasic curves could not be reliably fitted to a theoretical biding model. Indeed, previous NMR data and results from CD spectroscopy indicated that the event of metal ion binding to CIB2 is coupled with the protein folding process [7]. Therefore, the enthalpy changes measured by ITC under these conditions include various energetic contributions not limited to the metal ion binding process, but referring also to protein conformational changes and events associated with solvent reorganization; thus, they do not permit to estimate the equilibrium constant of individual sites for metal ions. NMR data indicate that the EF4 binding site has a lower affinity for Mg(II) than EF3 and demonstrate that the folding of CIB2 is driven by ion binding to EF3, which is the first site to be occupied by either Ca(II) or Mg(II). This should be considered together with the fact that, within the cell, Ca(II) and Mg(II) always co-exist, and while the concentration of Ca(II) may significantly change depending on the specific signaling event, Mg(II) is always present at relatively high concentration. We therefore sought to study the binding events from a structural and thermodynamic perspective under these conditions as well.

Table 1
Thermodynamic binding parameters obtained in the competition experiments of 10 mM Mg(II) or Ca(II) to the CIB2 preincubated with Ca(II) or Mg(II) and fit to a one-site binding site model. Values reported are the mean ± standard deviation of three technical replicates.

Titration	N (sites)	K_D (μM)	ΔH (kcal/mol)	-TΔS (kcal/mol)	ΔG (kcal/mol)
Ca(II) on MgMg-CIB2	1.23 ± 0.04	47 ± 7	-0.7 ± 0.3	-5.2 ± 0.3	-5.90 ± 0.09
Mg(II) on CaCa-CIB2	1.13 ± 0.12	81 ± 11	-0.8 ± 0.5	-4.8 ± 0.5	-5.59 ± 0.07

We used ITC to investigate the process of cation replacement in the metal binding sites when CIB2 was previously saturated with either Mg(II) or Ca(II) and combined them with NMR, which provides atomic-level details. Regardless of the presence of Mg(II) or Ca(II) bound to CIB2, the binding isotherms in the competition experiments were best fit to a single binding site model (Fig. 6A-B), suggesting that, in both cases, only an ion was replaced by the other one. This model was validated by titration NMR experiments. In order to report residue-specific conformational changes in response to Ca(II), we monitored the perturbations in amide chemical shifts in the ^{1}H-^{15}N HSQC spectrum of MgMg-CIB2 by adding increasing amounts of Ca(II). Only the backbone amides of the EF4 binding site experienced meaningful chemical shift perturbations upon addition of Ca(II) (Fig. 5B). Under these conditions, a second NMR signal appeared in the ^{1}H-^{15}N HSQC spectrum in slow exchange on the NMR time scale with the MgMg-CIB2 form. At the end of the Ca(II) titration the same chemical shifts of the residues of the EF4 binding site corresponding to the Ca(II)-bound specie were observed, whereas the resonances of the EF3 site were not affected. This behavior indicates that the Mg(II) ion bound to EF4 is substituted with Ca(II) and also demonstrates that Mg(II) is still bound to EF3, even in the presence of 2.4 mM Ca(II). On the contrary, the titration with Mg(II) of CIB2 in the presence of 1.2 mM Ca(II) led to the exchange of the metal only in the EF3-binding site. Indeed, when Ca(II)-bound CIB2 was titrated with increasing amounts of Mg(II), the resonances corresponding to the specie in which a Mg(II) ion is bound to EF3 was observed in the ^{1}H-^{15}N HSQC spectrum in slow exchange with the Ca(II)-bound specie. In particular, at 0.8 mM Mg(II), the resonances of EF3 correspond to the Mg(II)-bound state appear at the expenses of those corresponding to the Ca(II)-bound specie (Fig. 5C). Both titrations resulted in the end in the same ^{1}H-^{15}N HSQC spectrum, which represents the fingerprint of the MgCa-CIB2 species.

Taken together, these results definitely demonstrate that the EF3 and EF4 metal binding sites have a different preference for Mg(II) and Ca(II) ions and allow to attribute the dissociation equilibrium constants determined by ITC (K_D values) to specific sites, thus resulting in the K_{DMgEF3} and K_{DCaEF4} (Table 1). Combining therefore NMR data and ITC results, we could predict the thermodynamic parameters of the following reactions:

$$CaCa\text{-}CIB2 + Mg(II) \Leftrightarrow^{K_{DMgEF3}} MgCa\text{-}CIB2 + Ca(II) \quad (3)$$

and

$$MgMg\text{-}CIB2 + Ca(II) \Leftrightarrow^{K_{DCaEF4}} MgCa\text{-}CIB2 + Mg(II) \quad (4)$$

Interestingly, we found that the presence of Mg(II) still leads to a relatively low affinity for Ca(II) binding to EF4, (K_{DCaEF4} = 47 μM, Table 1); on the other hand, the presence of Ca(II) bound to CIB2 results in a relatively high Mg(II) binding affinity in EF3 (K_{DMgEF3} = 81 μM, Table 1). Thermodynamic parameters measured in either competitive binding experiments thus support a picture where the heterogeneous binding events of either a Ca(II) or a Mg(II) ion that lead to cation replacement are spontaneous in each initial bound conformation, entropy-driven (Table 1), and do not depend on the specific path, provided that CIB2 ends up in the same MgCa state. Indeed, in each competition experiment, the enthalpic and entropic contributions were very similar for both preincubated conditions (Table 1). The relatively high favorable entropy change that accompanies the ion exchange event can be ascribed to the conformational rearrangements of the protein, a phenomenon that has been described in other calcium sensor proteins [48–50], and to the important contribution attributed to the solvation/desolvation of the Mg(II) ion and the consequent release of water molecules from the bulk. It should be indeed noted that the radius of a hydrated Mg(II) ion increases significantly more than that of Ca(II) (~400-fold larger compared to ~25-fold larger, respectively) with the practical consequence that Mg(II) cannot be easily removed from its hydration shell [52].

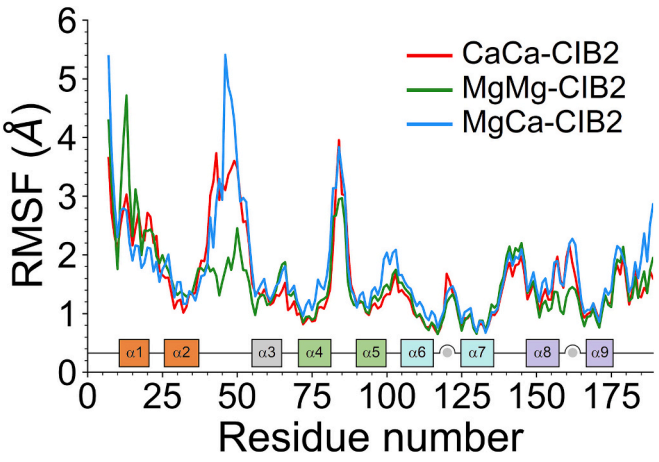

Fig. 7. Cα-RMSF profiles calculated over 1 μs MD simulations of CaCa-CIB2 (red), MgMg-CIB2 (green), and MgCa-CIB2 (blue). Inset shows the position of the 9 α-helices of CIB2, helices belonging to the same EF-hand (helix-loop-helix) motif are displayed in the same color, the positions where Ca(II) and Mg(II) ions are bound are represented as yellow circles.

3.5. Molecular dynamics simulations of CIB2 under different ion-loading conditions suggest inter-domain allosteric mechanisms involving Ca(II)-loaded EF4

The effects of Ca(II) and Mg(II) binding on protein structure and flexibility were investigated by running extensive 1 μs all-atom Molecular Dynamics (MD) simulations of CaCa-CIB2, MgMg-CIB2, and MgCa-CIB2, that is, all states that have been experimentally sampled in NMR and ITC experiments. All three systems exhibited a similar evolution over 1 μs of the Cα-RMSD calculated on the respective equilibrated structure, with values stably around ~3 Å after ~500 ns (Fig. S5). This suggests that the overall tertiary structure of CIB2 is not strictly dependent on the specific ion bound to either functional EF-hand, but rather on the presence of ions bound to EF3 and EF4, in line with the chemical shift differences exhibited by CaCa-CIB2 and MgMg-CIB2 in NMR experiments. Concerning protein flexibility, MgMg-CIB2 was overall the least flexible of the three states, especially in the α2-α3 loop (residues 35-55), and in the metal binding loop of EF4 (Fig. 7). On the other hand, the flexibility of the α2-α3 loop, belonging to the N-terminal domain of CIB2 and structurally apart from EF3 and EF4, appeared to depend on the metal ion bound to the binding motifs. Indeed, the exchange of the Mg(II) ion bound to EF4 with a Ca(II) ion resulted in a ~1 Å higher average RMSF (2.78 vs 1.72 Å) along the 35-55 region, with a peak represented by residues 46-49 displaying an RMSF >4 Å. The further Mg(II)/Ca(II) exchange in EF3, leading to the Ca(II)-loaded form, slightly stabilized the α2-α3 loop compared to the MgCa CIB2 form, with an average RMSF of 2.63 Å. Of interest, ^{15}N R_1 values, sensitive to local motions on the picosecond to nanosecond timescale, are higher than average for stretch 49-53 in both MgMg-CIB2 (Fig. 3) and MgCa-CIB2 (Fig. S6), as is often observed in the case of disordered loop regions of proteins. Moreover, signals linewidths of residues R49 and K50 are

Table 2
RMSF of metal cations bound to EF3 and EF4 of CIB2 calculated on 1 μs MD simulations.

Ion loading state	RMSF(Å) observed in each EF-hand	
	EF3	EF4
CaCa	0.96	1.75
MgMg	0.94	1.06
MgCa	1.06	1.61

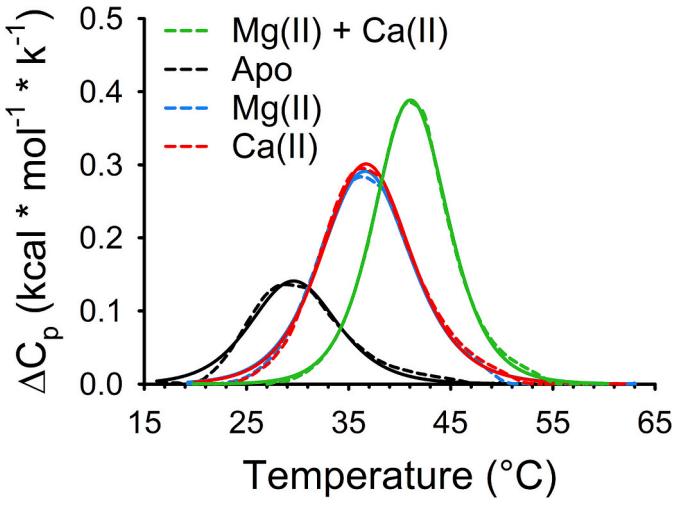

Fig. 8. Differential scanning calorimetry (DSC) experiments of 76 μM CIB2 in the absence and in the presence of metal ions. DSC thermograms of apo CIB2 in the presence of 1 mM EDTA (black dotted line), 1 mM Mg(II) (blue dotted line), 1 mM Ca(II) (red dotted line) and 1 mM Mg(II) + 1 mM Ca(II) (green dotted line), respectively, after baseline-correction and concentration-normalization. Superimposed colored lines represent the fitting function using a two-state transition model.

broad beyond detection, suggesting that the α2-α3 loop is affected both by fast dynamic processes typical of loops, and by dynamic processes occurring with much slower time constants, as is the case for allosteric transitions, which usually occur on the order of 10^{-6}-10^{0} s^{-1} [53]. Indeed, we monitored over 1 μs MD simulations the relative distances between K50 (representative of the flexible loop, Fig. S7A) and: i) K26 (Fig. S7B); ii) H33 (both located on the fairly rigid α2 helix, Fig. S7C); ii) and F90 (residing at the beginning of α2 helix, Fig. S7D); we observed that, in all three states, all three distances were relatively constant only for the first 50 ns of the trajectories. This suggests that the α2-α3 loop transiently adopts a range of low populated conformations in equilibrium characterized by the high structural flexibility observed by MD simulations, which cannot possibly be observed in the NMR exchange limit, which refers to a substantially different time scale [54].

We also sought to determine the flexibility of the metal cations bound to EF3 and EF4 in the different ion loading states by computing their RMSF; this permits to investigate the propensity of the ions to detach from the binding loop [55]. Mg(II) ions displayed on average ~1.4-fold lower RMSF compared to Ca(II) ions regardless of the ion-loading state (Table 2), hinting at a coordination geometry generally more favorable to Mg(II)-binding. In addition, ions bound to EF4 were found to fluctuate more within the ion binding loop with respect to their counterpart in EF3 (0.96 vs 1.75 Å, 0.94 vs 1.06 Å, and 1.06 vs 1.61 Å, Table 2), consistently with the higher flexibility exhibited by the entire EF4 ion-binding loop (Fig. 7) and substantially in line with heteronuclear NMR relaxation experiments (Figs. 3 and S6). Notably, such differences in RMSF were exacerbated when Ca(II) was bound to EF4 (1.75 Å and 1.61 Å vs 1.06 Å, Table 2). The heteronuclear NMR relaxation experiments conducted on MgCa-CIB2 also revealed that some

Table 3
Thermal stability of CIB2 in the absence of ions (apo, 1 mM EDTA) and in the presence of 1 mM Mg(II), 1 mM Ca(II), and 1 mM Mg(II) + 1 mM Ca(II), obtained by fit of DSC curves using a two-state transition model.

Condition	T_m (°C)	ΔH (kcal/mol)
Apo	29.70 ± 0.06	64.7 ± 0.9
Mg(II)	36.72 ± 0.02	64.7 ± 0.3
Ca(II)	36.81 ± 0.02	65.9 ± 0.5
Mg(II) + Ca(II)	41.14 ± 0.01	81.9 ± 0.3

residues belonging to the EF4 binding loop experience Rex contribution to R_2 values higher than that of MgMg-CIB2 (Fig. S6) suggesting an even more pronounced mobility in slow time scales of this loop, in line with MD data. Taken together, results from MD simulations suggest the existence of allosteric connections between the N- and C-terminal lobes of CIB2, which depend on the presence of Ca(II) bound to EF4 and mostly influence the mobility of the α2-α3 loop. This could have specific functional consequences that remain to be determined.

3.6. Differential scanning calorimetry (DSC) highlights the high stability of the MgCa-CIB2 state

It has long been known that, in the absence of cations, CIB2 forms a molten globule state deprived of tertiary structure, while the addition of either Mg(II) or Ca(II) induces a well-folded structure stabilizing the protein tertiary structure [8]. This has been directly proven by comparing the far- and near-UV CD spectra of apo-CIB2, and corroborated by NMR spectroscopy [7]. We used Differential Scanning Calorimetry (DSC) to probe whether and how the binding of cations increases the thermal stability of CIB2. Fig. 8 shows the DSC traces of the experimental data and the best-fitting results using a two-state transition model. Thermal denaturation data showed that the apo form of CIB2 is relatively unstable, with a melting temperature (T_m) of 29.7 °C (Table 3). This value is comparable with that obtained by monitoring the residual secondary structure of CIB2 upon thermal denaturation by CD spectroscopy (T_m = 35.1 °C), and the difference is consistent with the protein being in a molten globule state in the absence of cations [7]. A comparable stabilizing effect was observed upon addition of Mg(II) or Ca(II), with a shift of the thermograms towards a higher temperature (T_m = 36.7 °C and 36.8 °C for Mg(II) and Ca(II), respectively). Interestingly, we observed that in the presence of both cations the stability of CIB2 further increased the T_m by 4 °C (41.1 °C). In addition, when incubated with both Mg(II) and Ca(II) ions, CIB2 showed a remarkable (~16 kcal/mol) increase of denaturation enthalpy (Table 3), suggesting that specific and relatively strong interactions are formed when the EF3 and EF4 binding sites are occupied by Mg(II) and Ca(II), respectively. This is fully in line with NMR results, as in the state corresponding to MgMg-CIB2, EF4 appears not to be fully Mg(II)-bound, while CaCa-CIB2 is intrinsically unstable due to the lower affinity of Ca(II) for EF3; overall, this suggests that MgCa-CIB2 is likely to be the most biologically relevant state.

3.7. NMR characterization of the MgMg-CIB2 and MgCa-CIB2/α7B_M peptide interaction

Among the many biological partners identified [8], previous studies showed that CIB2 recognizes and binds the membrane-proximal region of the cytosolic tail of α7B integrin (from now on referred to as α7B_M peptide) [10]. Surface plasmon resonance suggested that CIB2 binds the α7B_M peptide with micromolar affinity and that the formation of a protein-peptide complex may drive the binding of a second CIB2 molecule [16]. To perform an atomic level characterization of the CIB2/α7B_M interaction, the ^{15}N labeled protein was titrated with increasing amount of peptide and the titration was followed by NMR spectroscopy. These experiments were performed both in the presence of Mg(II) alone

Fig. 9. Surface representation of MgMg-CIB2 protein. The exposed residues interacting with the α7β_M integrin peptide are shown in red and labeled.

and in the presence of both Mg(II) and Ca(II) ions.

Residues within MgMg-CIB2 exhibiting a combined chemical shift variation >0.03 ppm during titration with the α7B_M peptide are depicted onto the MgMg-CIB2 structural model in Fig. 9. Similarly, we observed protein-peptide interaction in the case of MgCa-CIB2. The chemical shift differences for both MgMg-CIB2 and MgCa-CIB2 are reported in Fig. S8. In both instances, the involved residues are located in the C-terminal domain of CIB2, showing that the recognition of this molecular target occurs with a similar interface, regardless of the cation bound to EF4.

To assess the oligomerization state of CIB2 in the presence of the α7B_M peptide and evaluate whether the interaction influences internal protein mobility, we performed heteronuclear relaxation experiments on the protein-peptide complexes. The average backbone ^{15}N longitudinal R_1 for MgMg-CIB2 and MgCa-CIB2 in the presence of 2 equivalents of α7B_M peptide were 1.5 ± 0.3 s^{-1} and 1.3 ± 0.3 s^{-1}, respectively. These values are comparable with those obtained for the isolated protein (1.3 ± 0.1 s^{-1} for MgMg-CIB2 and 1.3 ± 0.2 s^{-1} for MgCa-CIB2, respectively), indicating that the interaction with the peptide does not induce the dimerization of CIB2, which interacts with α7B_M as a monomer. The target-induced dimerization of CIB2 hypothesized in a previous study and based on surface plasmon resonance [16] could thus be an artefact due to the specific experimental on-chip conditions.

Interestingly, the stretch 138-148, located in the loop proceeding helix α8, maintained high flexibility in the ns-ps time scale, as evident by {^1H}-^{15}N heteronuclear NOE values lower than average 0.23 ± 0.04. These findings suggest that binding of α7B_M peptide does not introduce additional rigidity; on the contrary, the protein appears to be even more flexible upon interaction. Such behavior has been previously hypothesized by Near-UV CD spectroscopy measurements [7]. Considering that the homolog protein CIB1 allows a high degree of promiscuity in target recognition [56], the fact that CIB2 remains highly flexible upon target binding might play a role in protein function and contribute to the molecular recognition of a broad variety of proteins.

4. Conclusion

In this work, we presented a comprehensive analysis of the structural properties of CIB2 in the presence of Ca(II) and Mg(II) cations, which may represent a snapshot of the possible signaling states of the protein in different physiological contexts. By integrating high-resolution experimental data with calorimetric studies and molecular simulations, the main conclusion of our work is that among the possible occupancy states of its EF-hands, the one that sees EF3 occupied by an Mg(II) ion and EF4 occupied by a Ca(II) ion is the most likely. The MgCa-CIB2 state also shows remarkable stability, and appears to be the natural endpoint in the co-presence of the two metal cations, irrespective of the starting state, be it Ca(II)- or Mg(II)-loaded. The achievement of such a heterogeneous state of occupancy is rather unusual for a calcium-sensor protein and could be a feature that distinguishes CIB2 from other members of the CIB family. On the other hand, the protein's characteristic structural flexibility could be an essential element in ensuring the remarkable functional plasticity that suggests the involvement of CIB2 in many disparate physiological processes. In conclusion, although the apparent affinities for Ca(II) of CIB2's binding sites are relatively low when compared with those of other calcium sensors including CIB1 (0.5-1.9 μM [41,44]), the peculiarity of being partially bound to Mg(II) under physiological conditions may confer specific calcium-sensing capacities to CIB2. In addition, it cannot be ruled out that interaction with its many molecular targets may also significantly increase its affinity for Ca(II), as has been amply demonstrated for the ubiquitous calcium sensor calmodulin. It has been previously shown that target binding, i.e. α7B_M, can indeed increase the apparent affinity of CIB2 for Ca(II) of about 2.5-fold while at the same time decreasing that for Mg(II) [7]. Thorough biochemical and biophysical investigations of CIB2 in complex with its target are needed to assess the general validity of this hypothesis and clarify the mechanistic details.

CRediT authorship contribution statement

Gabriele Olivieri: Visualization, Methodology, Investigation. **Giuditta Dal Cortivo:** Visualization, Methodology, Investigation. **Rebecca Dal Conte:** Methodology, Investigation, Conceptualization. **Serena Zanzoni:** Writing – original draft, Methodology, Investigation. **Valerio Marino:** Writing – original draft, Investigation, Formal analysis. **Daniele Dell'Orco:** Writing – review & editing, Writing – original draft, Supervision, Funding acquisition, Conceptualization. **Francesca Cantini:** Writing – review & editing, Writing – original draft, Supervision, Funding acquisition, Conceptualization.

Declaration of competing interest

The authors declare that they have no known competing financial interests or personal relationships that could have appeared to influence the work reported in this paper.

Acknowledgements

The Centro Piattaforme Tecnologiche of the University of Verona is acknowledged for providing access to the computational and spectroscopic platforms. This study was supported by the Next Generation EU/Ministry of University and Research project: "A multiscale integrated approach to the study of the nervous system in health and disease (MNESYS)", CUP B33C22001060002, PE00000006 missione 4, componente 2, investimento 1.3 and by "the European Union-NextGenerationEU-National Recovery and Resilience Plan, Mission 4 Component 2-Investment 1.5-THE-Tuscany Health Ecosystem-ECS00000017-CUP B83C22003920001. Support was obtained from the 8th Instruct Internship program (APPID 1732) and visits identified with the following PID: 14003 (3 visits), 17698 (one visit), 19345 (one visit),

24055 (2 visits) and 26603 (one visit).

Appendix A. Supplementary data

Supplementary data to this article can be found online at https://doi.org/10.1016/j.ijbiomac.2024.138003.

References

[1] H.R. Gentry, A.U. Singer, L. Betts, C. Yang, J.D. Ferrara, J. Sondek, L.V. Parise, Structural and biochemical characterization of CIB1 delineates a new family of EF-hand-containing proteins, J. Biol. Chem. 280 (9) (2005) 8407–8415.

[2] H. Huang, J.N. Bogstie, H.J. Vogel, Biophysical and structural studies of the human calcium- and integrin-binding protein family: understanding their functional similarities and differences, Biochem. Cell Biol. 90 (5) (2012) 646–656.

[3] X. Liang, X. Qiu, G. Dionne, C.L. Cunningham, M.L. Pucak, G. Peng, Y.-H. Kim, A. Lauer, L. Shapiro, U. Müller, CIB2 and CIB3 are auxiliary subunits of the mechanotransduction channel of hair cells, Neuron 109 (13) (2021) 2131–2149.e15.

[4] D. Dell'Orco, K.W. Koch, M.R. Kreutz, J.R. Naranjo, B. Schwaller, Editorial: neuronal calcium sensors in health and disease, Front. Mol. Neurosci. 12 (2019) 278.

[5] S. Riazuddin, I.A. Belyantseva, A.P. Giese, K. Lee, A.A. Indzhykulian, S. P. Nandamuri, R. Yousaf, G.P. Sinha, S. Lee, D. Terrell, R.S. Hegde, R.A. Ali, S. Anwar, P.B. Andrade-Elizondo, A. Sirmaci, L.V. Parise, S. Basit, A. Wali, M. Ayub, M. Ansar, W. Ahmad, S.N. Khan, J. Akram, M. Tekin, S. Riazuddin, T. Cook, E.K. Buschbeck, G.I. Frolenkov, S.M. Leal, T.B. Friedman, Z.M. Ahmed, Alterations of the CIB2 calcium- and integrin-binding protein cause usher syndrome type 1J and nonsyndromic deafness DFNB48, Nat. Genet. 44 (11) (2012) 1265–1271.

[6] H. Kawasaki, S. Nakayama, R.H. Kretsinger, Classification and evolution of EF-hand proteins, Biometals 11 (4) (1998) 277–295.

[7] R. Vallone, G. Dal Cortivo, M. D'Onofrio, D. Dell'Orco, Preferential binding of Mg2+ over Ca2+ to CIB2 triggers an allosteric switch impaired in usher syndrome type 1J, Front. Mol. Neurosci. 11 (2018).

[8] G. Dal Cortivo, D. Dell'Orco, Calcium- and integrin-binding protein 2 (CIB2) in physiology and disease: bright and dark sides, Int. J. Mol. Sci. 23 (7) (2022) 3552.

[9] J.C. Denofrio, W. Yuan, B.R. Temple, H.R. Gentry, L.V. Parise, Characterization of calcium- and integrin-binding protein 1 (CIB1) knockout platelets: potential compensation by CIB family members, Thromb. Haemost. 100 (5) (2008) 847–856.

[10] M. Häger, M.G. Bigotti, R. Meszaros, V. Carmignac, J. Holmberg, V. Allamand, M. Åkerlund, S. Kalamajski, A. Brancaccio, U. Mayer, M. Durbeej, Cib2 binds integrin α7Bβ1D and is reduced in laminin α2 chain-deficient muscular dystrophy, J. Biol. Chem. 283 (36) (2008) 24760–24769.

[11] A. Jacoszek, A. Pollak, R. Ploski, M. Oldak, Advances in genetic hearing loss: CIB2 gene, Eur. Arch. Otorhinolaryngol. 274 (4) (2017) 1791–1795.

[12] A.P.J. Giese, Y.Q. Tang, G.P. Sinha, M.R. Bowl, A.C. Goldring, A. Parker, M. J. Freeman, S.D.M. Brown, S. Riazuddin, R. Fettiplace, W.R. Schafer, G. I. Frolenkov, Z.M. Ahmed, CIB2 interacts with TMC1 and TMC2 and is essential for mechanotransduction in auditory hair cells, Nat. Commun. 8 (1) (2017) 43.

[13] Y. Wang, J. Li, X. Yao, W. Li, H. Du, M. Tang, W. Xiong, R. Chai, Z. Xu, Loss of CIB2 causes profound hearing loss and abolishes Mechanoelectrical transduction in mice, Front Mol Neurosci 10 (2017) 401.

[14] K. Yan, W. Zong, H. Du, X. Zhai, R. Ren, S. Liu, W. Xiong, Y. Wang, Z. Xu, BAIAP2L2 is required for the maintenance of mechanotransducing stereocilia of cochlear hair cells, J. Cell. Physiol. 237 (1) (2022) 774–788.

[15] C.Z. Seco, A.P. Giese, S. Shafique, M. Schraders, A.M. Oonk, M. Grossheim, J. Oostrik, T. Strom, R. Hegde, E. van Wijk, G.I. Frolenkov, M. Azam, H.G. Yntema, R.H. Free, S. Riazuddin, J.B. Verheij, R.J. Admiraal, R. Qamar, Z.M. Ahmed, H. Kremer, Novel and recurrent CIB2 variants, associated with nonsyndromic deafness, do not affect calcium buffering and localization in hair cells, Eur. J. Hum. Genet. 24 (4) (2016) 542–549.

[16] G. Dal Cortivo, V. Marino, C. Iacobucci, R. Vallone, C. Arlt, A. Rehkamp, A. Sinz, D. Dell'Orco, Oligomeric state, hydrodynamic properties and target recognition of human calcium and integrin binding protein 2 (CIB2), Sci. Rep. 9 (1) (2019).

[17] S. Sethna, P.A. Scott, A.P.J. Giese, T. Duncan, X. Jian, S. Riazuddin, P.A. Randazzo, T.M. Redmond, S.L. Bernstein, S. Riazuddin, Z.M. Ahmed, CIB2 regulates mTORC1 signaling and is essential for autophagy and visual function, Nat. Commun. 12 (1) (2021) 3906.

[18] X. Wang, Y. Yang, W.Q. Cai, Y. Lu, The relationship of sphingosine kinase 1 with Pyroptosis provides a new strategy for tumor therapy, Front. Immunol. 11 (2020) 574990.

[19] R. Keller, The computer aided resonance assignment tutorial (2004) 1–81.

[20] Y. Shen, A. Bax, Protein backbone and sidechain torsion angles predicted from NMR chemical shifts using artificial neural networks, J. Biomol. NMR 56 (3) (2013) 227–241.

[21] R. Ishima, D.A. Torchia, Nat. Struct. Biol. 7 (9) (2000) 740–743.

[22] G. Lipari, A. Szabo, Model-free approach to the interpretation of nuclear magnetic resonance relaxation in macromolecules. 1. Theory and range of validity, J. Am. Chem. Soc. 104 (17) (2002) 4546–4559.

[23] C. Charlier, S.F. Cousin, F. Ferrage, Protein dynamics from nuclear magnetic relaxation, Chem. Soc. Rev. 45 (9) (2016) 2410–2422.

[24] J. García de la Torre, M.L. Huertas, B. Carrasco, HYDRONMR: prediction of NMR relaxation of globular proteins from atomic-level structures and hydrodynamic calculations, J. Magn. Reson. 147 (1) (2000) 138–146.

[25] M. Mirdita, K. Schütze, Y. Moriwaki, L. Heo, S. Ovchinnikov, M. Steinegger, ColabFold: making protein folding accessible to all, Nat. Methods 19 (6) (2022) 679–682.

[26] J. Jumper, R. Evans, A. Pritzel, T. Green, M. Figurnov, O. Ronneberger, K. Tunyasuvunakool, R. Bates, A. Žídek, A. Potapenko, A. Bridgland, C. Meyer, S.A. A. Kohl, A.J. Ballard, A. Cowie, B. Romera-Paredes, S. Nikolov, R. Jain, J. Adler, T. Back, S. Petersen, D. Reiman, E. Clancy, M. Zielinski, M. Steinegger, M. Pacholska, T. Berghammer, S. Bodenstein, D. Silver, O. Vinyals, A.W. Senior, K. Kavukcuoglu, P. Kohli, D. Hassabis, Highly accurate protein structure prediction with AlphaFold, Nature 596 (7873) (2021) 583–589.

[27] M. Varadi, S. Anyango, M. Deshpande, S. Nair, C. Natassia, G. Yordanova, D. Yuan, O. Stroe, G. Wood, A. Laydon, A. Zidek, T. Green, K. Tunyasuvunakool, S. Petersen, J. Jumper, E. Clancy, R. Green, A. Vora, M. Lutfi, M. Figurnov, A. Cowie, N. Hobbs, P. Kohli, G. Kleywegt, E. Birney, D. Hassabis, S. Velankar, AlphaFold protein structure database: massively expanding the structural coverage of protein-sequence space with high-accuracy models, Nucleic Acids Res. 50 (D1) (2022) D439–D444.

[28] T. Herrmann, P. Güntert, K. Wüthrich, J. Biomol. NMR 24 (3) (2002) 171–189.

[29] I.B. Trindade, A. Coelho, F. Cantini, M. Piccioli, R.O. Louro, NMR of paramagnetic metalloproteins in solution: Ubi venire, quo vadis? J. Inorg. Biochem. 234 (2022) 111871.

[30] A. Avesani, V. Marino, S. Zanzoni, K.W. Koch, D. Dell'Orco, Molecular properties of human guanylate cyclase-activating protein 2 (GCAP2) and its retinal dystrophy-associated variant G157R, J. Biol. Chem. 296 (2021) 100619.

[31] S. Abbas, K.W. Koch, Quantitative determination of ca(2+)-binding to ca(2+)-sensor proteins by isothermal titration calorimetry, Bio-Protoc. 10 (7) (2020) e3580.

[32] H. Li, A.D. Robertson, J.H. Jensen, Very fast empirical prediction and rationalization of protein pKa values, Proteins: Structure, Function, and Bioinformatics 61 (4) (2005) 704–721.

[33] M.J. Abraham, T. Murtola, R. Schulz, S. Páll, J.C. Smith, B. Hess, E. Lindahl, GROMACS: high performance molecular simulations through multi-level parallelism from laptops to supercomputers, SoftwareX 1-2 (2015) 19–25.

[34] J. Huang, S. Rauscher, G. Nawrocki, T. Ran, M. Feig, B.L. de Groot, H. Grubmüller, A.D. MacKerell, CHARMM36m: an improved force field for folded and intrinsically disordered proteins, Nat. Methods 14 (1) (2016) 71–73.

[35] V. Marino, S. Sulmann, K.-W. Koch, D. Dell'Orco, Structural effects of Mg2+ on the regulatory states of three neuronal calcium sensors operating in vertebrate phototransduction, Biochimica et Biophysica Acta (BBA) - molecular, Cell Res. 1853 (9) (2015) 2055–2065.

[36] V. Marino, D. Dell'Orco, Allosteric communication pathways routed by Ca2+/Mg2+ exchange in GCAP1 selectively switch target regulation modes, Sci. Rep. 6 (1) (2016).

[37] V. Marino, D. Dell'Orco, Evolutionary-conserved allosteric properties of three neuronal calcium sensor proteins, Frontiers in Molecular Neuroscience 12 (2019).

[38] H. Huang, H. Ishida, A.P. Yamniuk, H.J. Vogel, Solution structures of Ca2+-CIB1 and Mg2+-CIB1 and their interactions with the platelet integrin αIIb cytoplasmic domain, J. Biol. Chem. 286 (19) (2011) 17181–17192.

[39] E.F. Pettersen, T.D. Goddard, C.C. Huang, G.S. Couch, D.M. Greenblatt, E.C. Meng, T.E. Ferrin, UCSF Chimera–a visualization system for exploratory research and analysis, J. Comput. Chem. 25(13) (2004) 1605–12.

[40] A. Lewit-Bentley, S. Réty, EF-hand calcium-binding proteins, Curr. Opin. Struct. Biol. 10 (6) (2000) 637–643.

[41] A.P. Yamniuk, L.T. Nguyen, T.T. Hoang, H.J. Vogel, Metal ion binding properties and conformational states of calcium- and integrin-binding protein, Biochemistry 43 (9) (2004) 2558–2568.

[42] N.S. Edmunds, A.G. Genc, L.J. McGuffin, Benchmarking of AlphaFold2 accuracy self-estimates as indicators of empirical model quality and ranking: a comparison with independent model quality assessment programmes, Bioinformatics 40 (8) (2024).

[43] D. Gottstein, D.K. Kirchner, P. Guntert, Simultaneous single-structure and bundle representation of protein NMR structures in torsion angle space, J. Biomol. NMR 52 (4) (2012) 351–364.

[44] A.P. Yamniuk, D.M. Silver, K.L. Anderson, S.R. Martin, H.J. Vogel, Domain stability and metal-induced folding of calcium- and integrin-binding protein 1, Biochemistry 46 (24) (2007) 7088–7098.

[45] S.M. Gagne, M.X. Li, B.D. Sykes, Mechanism of direct coupling between binding and induced structural change in regulatory calcium binding proteins, Biochemistry 36 (15) (1997) 4386–4392.

[46] Z. Grabarek, Insights into modulation of calcium signaling by magnesium in calmodulin, troponin C and related EF-hand proteins, Biochim. Biophys. Acta 1813 (5) (2011) 913–921.

[47] S.K. Drake, J.J. Falke, Kinetic tuning of the EF-hand calcium binding motif: the gateway residue independently adjusts (i) barrier height and (ii) equilibrium, Biochemistry 35 (6) (1996) 1753–1760.

[48] D. Dell'Orco, K.W. Koch, Fingerprints of calcium-binding protein conformational dynamics monitored by surface Plasmon resonance, ACS Chem. Biol. 11 (9) (2016) 2390–2397.

[49] D. Dell'Orco, S. Sulmann, S. Linse, K.W. Koch, Dynamics of conformational Ca2+−switches in signaling networks detected by a planar plasmonic device, Anal. Chem. 84 (6) (2012) 2982–2989.

[50] D. Dell'Orco, M. Muller, K.W. Koch, Quantitative detection of conformational transitions in a calcium sensor protein by surface plasmon resonance, Chem. Commun. (Camb.) 46 (39) (2010) 7316–7318.
[52] M.E. Maguire, J.A. Cowan, Magnesium chemistry and biochemistry, Biometals 15 (3) (2002) 203–210.
[53] J.A. McCammon, S.C. Harvey, Dynamics of Proteins and Nucleic Acids, Cambridge University Press1988.
[54] V.P. Tiwari, D. De, N. Thapliyal, L.E. Kay, P. Vallurupalli, Beyond slow two-state protein conformational exchange using CEST: applications to three-state protein interconversion on the millisecond timescale, J. Biomol. NMR 78 (1) (2024) 39–60.
[55] A. Avesani, L. Bielefeld, N. Weisschuh, V. Marino, P. Mazzola, K. Stingl, T.B. Haack, K.-W. Koch, D. Dell'Orco, Molecular properties of human guanylate cyclase-activating protein 3 (GCAP3) and its possible association with retinitis Pigmentosa, Int. J. Mol. Sci. 23 (6) (2022) 3240.
[56] T.M. Leisner, T.C. Freeman, J.L. Black, L.V. Parise, CIB1: a small protein with big ambitions, FASEB J. 30 (8) (2016) 2640–2650.
[57] M.P. Williamson, Using chemical shift perturbation to characterise ligand binding, Prog. Nucl. Magn. Reson. Spectrosc. 73 (2013) 1–16.